

# **Technical Report**

## **III-Nitride Visible- and Solar-Blind Avalanche Photodiodes**

**Contract No: FA9550-07-1-0326**

**(December, 2007)**

**Program Manager:**

**Dr. Donald Silversmith – Air Force Office of Scientific  
Research**

**Principal Investigator: Professor Manijeh Razeghi**

**Center for Quantum Devices**

Electrical Engineering and Computer Science Department

Northwestern University

2220 Campus Drive: Cook Hall Rm. 4051; Evanston, IL 60208

Tel: (847) 491-7251, Fax: (847) 467-1817

Email: [razeghi@eecs.northwestern.edu](mailto:razeghi@eecs.northwestern.edu)

<b>REPORT DOCUMENTATION PAGE</b>			Form Approved OMB NO. 0704-0188	
Public Reporting burden for this collection of information is estimated to average 1 hour per response, including the time for reviewing instructions, searching existing data sources, gathering and maintaining the data needed, and completing and reviewing the collection of information. Send comment regarding this burden estimates or any other aspect of this collection of information, including suggestions for reducing this burden, to Washington Headquarters Services, Directorate for information Operations and Reports, 1215 Jefferson Davis Highway, Suite 1204, Arlington, VA 22202-4302, and to the Office of Management and Budget, Paperwork Reduction Project (0704-0188,) Washington, DC 20503.				
1. AGENCY USE ONLY ( Leave Blank)		2. REPORT DATE 12/18/07		3. REPORT TYPE AND DATES COVERED Final Technical Report 4/07-11/07
4. TITLE AND SUBTITLE  III-Nitride Visible- and Solar-Blind Avalanche Photodiodes			5. FUNDING NUMBERS FA9550-07-1-0326	
6. AUTHOR(S) M. Razeghi				
7. PERFORMING ORGANIZATION NAME(S) AND ADDRESS(ES) Northwestern University Center for Quantum Devices 2220 Campus Drive, Room 4051 Evanston, IL 60208			8. PERFORMING ORGANIZATION REPORT NUMBER 0650-350-S408	
9. SPONSORING / MONITORING AGENCY NAME(S) AND ADDRESS(ES)  U.S. Air Force Office of Scientific Research 875 N. Randolph Street Arlington, VA 22203-1954			10. SPONSORING / MONITORING AGENCY REPORT NUMBER	
11. SUPPLEMENTARY NOTES The views, opinions and/or findings contained in this report are those of the author(s) and should not be construed as an official Department of the Air Force position, policy or decision, unless so designated by other documentation.				
12 a. DISTRIBUTION / AVAILABILITY STATEMENT  Approved for public release; distribution unlimited.			12 b. DISTRIBUTION CODE	
13. ABSTRACT (Maximum 200 words)  There is a need for single photon detectors for a variety of scientific, military, and civilian applications. Compared to photomultiplier tubes or superconducting single photon detectors, the use of Geiger-mode avalanche photodiodes (APDs) presents advantages such as lower operation voltages, reduced sizes, and reduced need for cooling, which may enable the fabrication of more compact, lower power, and all-solid-state APD/CMOS integrated arrays. APDs based on wide-band-gap semiconductors are of special interest when there is a need for reliable ultraviolet detection with single photon counting capabilities. The tunable response of AlGaIn detectors allows for solar- to visible-blind performances within the same material system, without the need of filters.  We report on the growth, fabrication, and characterization of back-illuminated GaN APDs on thick AlN templates. Comparison of the performance of these same devices under front and back illumination allows us to reach a better understanding of carrier multiplication in this material and to determine experimentally both electron and hole ionization coefficients. Devices of various mesa sizes were fabricated and the effects of increased area on device performance were studied. Finally, devices were characterized in Geiger mode to evaluate their capabilities for single-photon detection.				
14. SUBJECT TERMS III-Nitrides, Ultraviolet, Avalanche Photodiodes, GaN, Geiger Mode			15. NUMBER OF PAGES  21	
			16. PRICE CODE	
17. SECURITY CLASSIFICATION OR REPORT <b>UNCLASSIFIED</b>	18. SECURITY CLASSIFICATION ON THIS PAGE <b>UNCLASSIFIED</b>	19. SECURITY CLASSIFICATION OF ABSTRACT <b>UNCLASSIFIED</b>	20. LIMITATION OF ABSTRACT  <b>UL</b>	

# Table of Contents

1	Introduction .....	3
2	Growth, Material Characterization and Device Processing .....	3
	2.1 Material Growth and Characterization. ....	3
	2.2 Device Processing. ....	7
	2.3 Low-Bias Device Characteristics. ....	7
3	Carrier Multiplication in Gallium Nitride .....	8
	3.1 Experimental Determination of the Critical Electric Field. ....	8
	3.2 Multiplication Gain Measurements and Determination of Ionization Coefficients. ....	10
	3.3 Noise measurements.....	11
	3.4 Summary. ....	12
4	Linear-mode operation of back-illuminated GaN APDs.....	12
	4.1. Scaling in back-illuminated GaN APDs.....	12
	4.2. Spectral response.....	13
	4.4. Temperature dependence of the breakdown voltage.....	15
	4.5. Summary. ....	16
5	Geiger-mode operation of back-illuminated GaN APDs .....	16
	5.1 Experimental Set-Up.....	16
	5.2 Spectral Response. ....	17
	5.3 Single Photon Detection Efficiency and Dark Count Rate. ....	18
	5.4 Summary. ....	19
6	Publications Resulting From This Project.....	19
7	References .....	20

# 1 Introduction

There is a need for single photon detectors for a variety of scientific, military, and civilian applications including free-space optical communications, quantum computing, environment monitoring, astrophysics, or biological agent detection.[1] Compared to photomultiplier tubes or superconducting single photon detectors, the use of Geiger-mode avalanche photodiodes (APDs) presents some advantages such as lower operation voltages, much reduced sizes, and no need for cooling to very low temperatures, which may enable the fabrication of more compact, lower power, and all-solid-state APD/CMOS integrated arrays.[2] Avalanche photodiodes based on wide-band-gap semiconductors are of special interest when there is a need for reliable ultraviolet (UV) detection with single photon counting capabilities. Materials such as SiC, AlGa<sub>N</sub>, or diamond present optoelectrical properties with intrinsic advantages for visible-blind UV detection, potentially outperforming other narrow-band-gap counterparts that require extensive filtering. In particular, the tunable response of AlGa<sub>N</sub> detectors allows us to accomplish solar- to visible-blind performances with the same material system without the need of filters, as well as to match specific bands of biological interest within the 200-360 nm range.[3,4] Geiger-mode operation under gated quenching has been previously demonstrated in front-illuminated GaN APDs with a single photon detection efficiency (SPDE) of 13% at a dark count rate of 400 kHz in devices with an area of 1075  $\mu\text{m}^2$ . [5] However, two of the major problems with GaN APDs are the rapid increase of the dark current with area and the consequent limitation of the maximum achievable gain, which have prevented the operation of larger area devices in Geiger mode. In contrast, SiC devices have shown a low dark count rate of 28 kHz for 7854  $\mu\text{m}^2$  devices but have done this with a lower SPDE of only 3.6%. [6]

In this document, we report on the growth, fabrication, and characterization of back-illuminated GaN APDs on thick AlN templates. Comparison of the performance of these same devices under front and back illumination allows us to reach a better understanding of carrier multiplication in this material and to determine experimentally both electron and hole ionization coefficients. Devices of various mesa sizes were fabricated and the effects of increased area on device performance were studied. Finally, devices were characterized in Geiger mode to evaluate their capabilities for single-photon detection.

## 2 Growth, Material Characterization and Device Processing

### 2.1 *Material Growth and Characterization.*

The material was grown in an AIXTRON 200/4-HT horizontal flow low-pressure metalorganic chemical vapor deposition reactor. Double side polished basal plane (00.1) sapphire was used as the substrate in order to allow for the realization of back-illuminated photodetectors. The key to achieving high quality back-illuminated GaN APDs consists

of first being able to attain the highest quality AlN epilayers possible and then GaN epilayers.

To do so, growth on the sapphire substrate was nucleated with a thin 200 Å low-temperature AlN buffer layer. On top of this a 0.5~0.6 µm thick high quality AlN template layer was grown by atomic layer epitaxy[7] at a temperature of ~1300°C. Figure 1 (left) shows a representative atomic force microscopy (AFM) imaging of the resulting AlN layer. The rms surface roughness was less than 1 Å for a 5×5 µm<sup>2</sup> scan area. Figure 1 (right) shows the room temperature photoluminescence of such AlN epilayers, confirming the high quality of the films. Open detector x-ray diffraction measurements yielded a (00.2) symmetric peak linewidth of ~40 arcsec and a (10.5) asymmetric peak linewidth of ~240 arcsec. At the origin of this high quality AlN is the good control of the buffer/substrate interface in spite of an existing 13.2 % effective lattice mismatch. Theoretical crystallographic models of such interface have been developed earlier[8,9] to determine how the lattice mismatch would be relaxed through the periodic formation of misfit dislocations every 9 atomic planes of sapphire and 8 atomic planes of AlN along the <10.0> direction of AlN. The modeled cross-section is shown in Figure 2 (left). This model was experimentally confirmed through imaging of the cross section between the AlN buffer and the basal plane sapphire substrate using high resolution transmission electron microscopy (HRTEM), Figure 2(right).

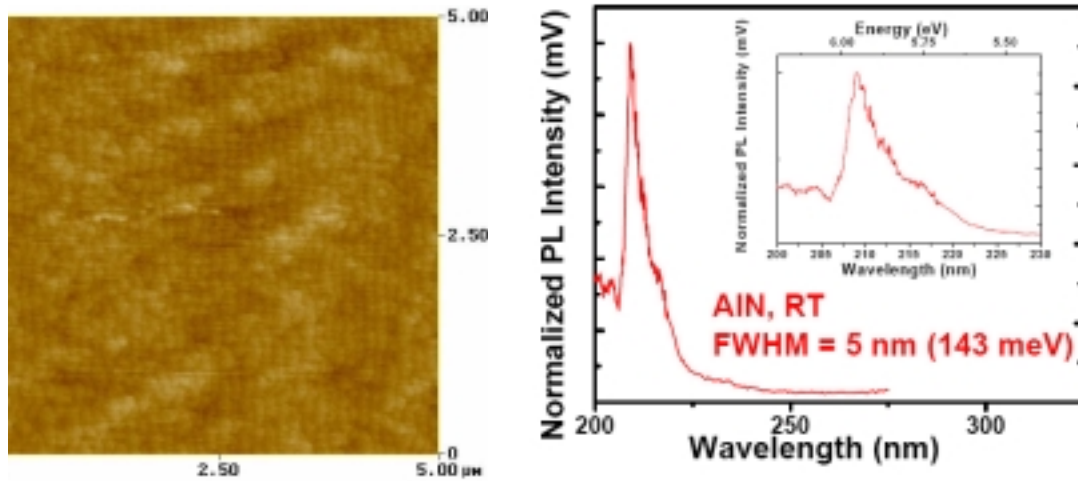


**Figure 1. (Left) Atomic force microscopy imaging of the surface of a high quality AlN template layer grown on basal plane sapphire substrate. The vertical scale is 1 nm. (Right) Room temperature photoluminescence of a high quality AlN layer (inset)**

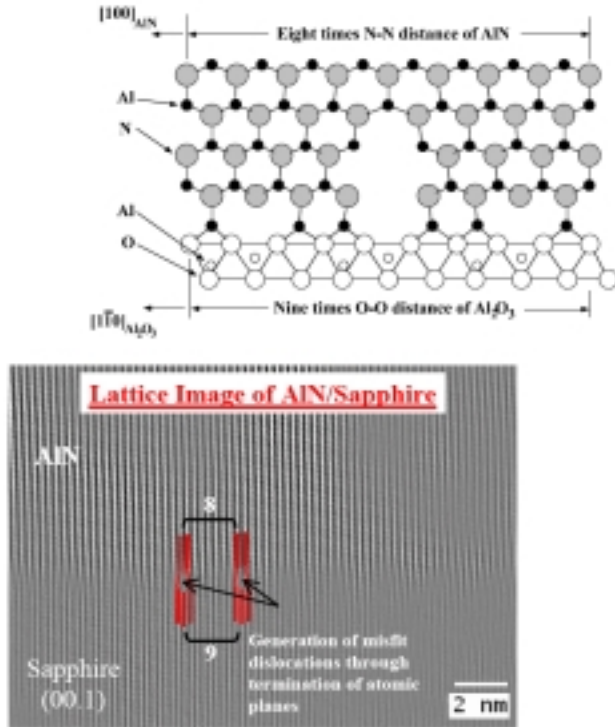


**Figure 2. (Left) Schematic crystallographic model of the cross-section between AlN and basal plane sapphire along the  $\langle 10.0 \rangle$  direction of AlN. (Right) High resolution cross-section TEM imaging of the same interface.**

The quality of GaN epilayers grown on such AlN templates was subsequently assessed. GaN films with  $0.5\sim 1.5\ \mu\text{m}$  thickness were deposited on top of the AlN templates. The layer surfaces were very smooth with very few observable dislocation termination pits, as shown in AFM imaging in Figure 3. The rms surface roughness was only  $1.29\ \text{\AA}$  for a  $5\times 5\ \mu\text{m}^2$  scan area. Open detector x-ray diffraction measurements yielded a (00.2) symmetric peak linewidth of  $\sim 82\ \text{arcsec}$  as shown in Figure 4 (left). The typical room temperature photoluminescence spectrum was measured using a frequency doubled argon-ion laser ( $\lambda=244\ \text{nm}$ ) and is shown in Figure 4 (right). The peak luminescence occurred at  $361\ \text{nm}$  with a linewidth of  $\sim 40\ \text{meV}$  and no yellow defect related luminescence was observed. Undoped GaN epilayers exhibited a room temperature mobility of  $450\sim 500\ \text{cm}^2/\text{V}\cdot\text{s}$  for a residual carrier concentration of  $n\sim 10^{16}\ \text{cm}^{-3}$ . N-type and p-type doping of these layers yielded carrier concentrations of  $1\sim 2\times 10^{18}\ \text{cm}^{-3}$ .

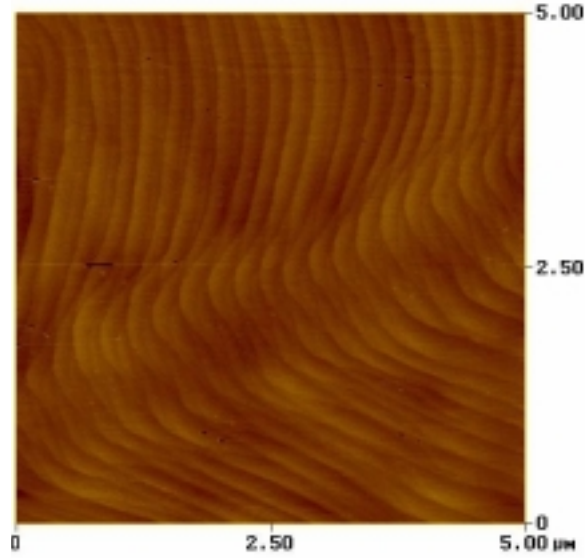


Figure 3. Atomic force microscopy imaging of the surface of a high quality GaN grown on an AlN template. The vertical scale is 2.2 nm.

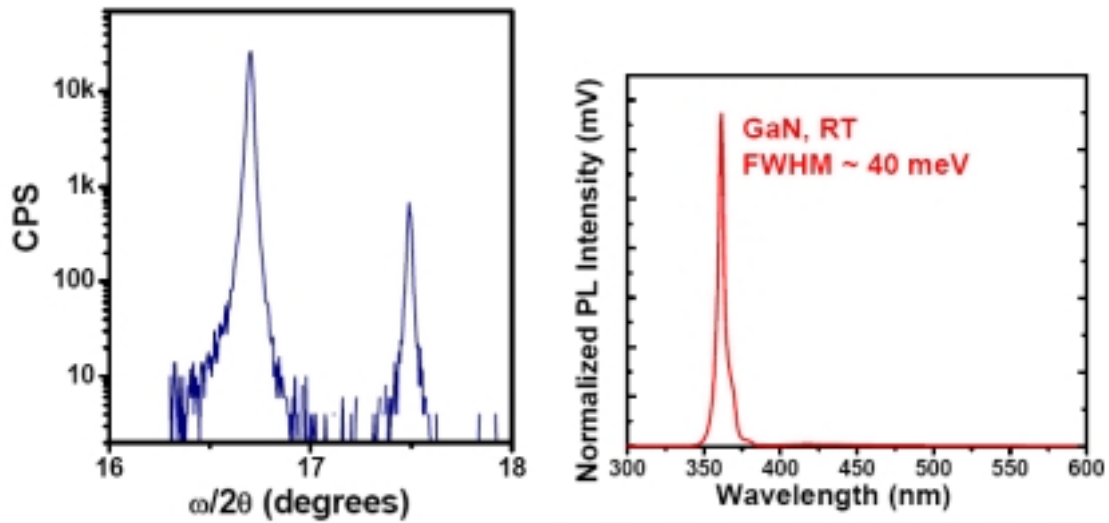


Figure 4. (Left) Open detector x-ray diffraction spectrum and (Right) room temperature photoluminescence spectrum of a 1.5  $\mu\text{m}$  GaN epilayer grown on high quality AlN template on sapphire substrates.

These calibrated GaN epilayers were used as building blocks for the back-illuminated GaN p-i-n avalanche photodiodes reported here. The structures consisted of a p-type GaN epilayer, on undoped i-GaN on n-type GaN, all grown on the high quality 0.5-0.6  $\mu\text{m}$  AlN template on sapphire. Several devices were realized with different GaN layer thicknesses. The thickness of the p-type GaN:Mg layer ranged from 100 to  $\sim 300$  nm, while the thickness of the undoped i-GaN region was varied from 50 to 200 nm, and the n-type GaN:Si layer thickness ranged from 100 to 400 nm. Although designed for back illumination, they can be measured under both back and front illumination. Unlike other reports of avalanche photodiodes, the total thickness of these devices, including template, did not exceed 1.5  $\mu\text{m}$ . Similar GaN p-i-n structures were also realized on 3  $\mu\text{m}$

thick n-type GaN:Si templates on sapphire for comparison purposes. These photodiodes can only be operated under front-illumination because of the high optical absorption from the underlying GaN:Si template layer.

## 2.2 Device Processing.

All samples were first rapid thermally annealed at 1000 °C for 30 seconds under dry N<sub>2</sub> to activate the magnesium in the p-type GaN:Mg layers. The material was patterned into an array of 25 µm × 25 µm square mesas using electron cyclotron resonance (ECR-RF) dry etching to reach the n-type GaN:Si contact layer. A thin 30 Å Ni / 30 Å Au layer was deposited on top of the mesas and annealed under ambient air at 500 °C for 10 minutes in order to form ohmic contacts to the p-type material on top of the device. A 400 Å Ti / 1200 Å Au metal layer was deposited on the GaN:Si layer to form the common n-type contact and on top of the thin Ni/Au as a thick metal contact. The devices were finally covered with 300 nm of SiO<sub>2</sub> deposited by plasma enhance chemical vapor deposition to help protect the mesas and prevent premature breakdown of the devices; windows were opened via wet etching. An illustration of a typical single diode out of the array is shown in Figure 5.

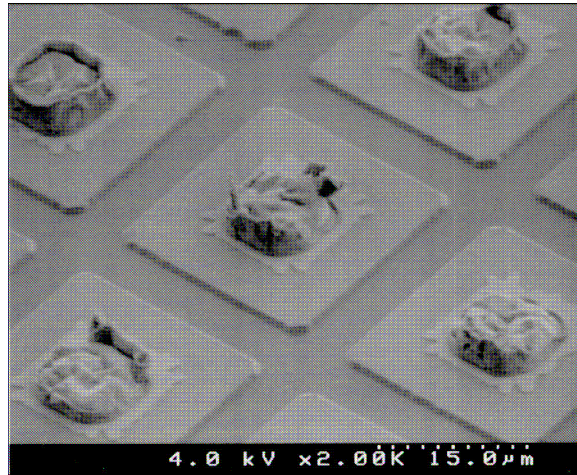


Figure 5. Scanning electron micrograph of an APD after processing. The common n-contact, not shown, is far removed from the mesas to avoid air breakdown of the devices. Indium bumps are also shown on these devices making them suitable for fabrication of APD arrays.

## 2.3 Low-Bias Device Characteristics.

A typical current-voltage (*I-V*) curve of a photodiode fabricated on an AlN template is shown in Figure 6 (left). The diodes exhibited a turn on voltage of 4.4-6.2 V. The diodes had very low dark currents at the ~10 fA noise floor limit of the curve tracer used to record these *I-V* curves, up to ~10 V reverse bias. The ideal diode equation, shown below, was used to fit the forward bias data.



$I_f = C \times \exp\left(\frac{qV}{nkT}\right)$	<b>Equation 1</b>
--	-------------------

where  $q$  is the charge of an electron,  $k$  is the Boltzmann constant,  $T$  is the temperature, and  $C$  a constant. This fitting allows the extraction an ideality factor,  $n$ , which can provide insight into the conduction mechanisms operating in these photodetectors. The ideality diode equation arises from the combination of the equations for diffusion current and recombination current: the two currents that usually dominate the diode current, and the ideality factor is expected to have a value between 1 and 2. Whereas if  $n$  is closer to 1, then diffusion current dominates and if  $n$  is closer to 2 then recombination current dominates. The ideality factor of these photodiodes ranged from a little below 2 to 4.

The series resistance of diodes on AlN templates was calculated and yielded values ranging from 450 to 3000  $\Omega$ , and scaled with the inverse of the  $n$ -type GaN layer thickness, which suggests that there was not a significant parallel conduction path contribution from the GaN/AlN interface.

A typical  $I$ - $V$  characteristic of photodiodes fabricated on GaN templates is shown in Figure 6 (right). The diode turn on voltage was about 4.2 V. These devices also exhibited a very low dark current up to ~10 V reverse bias. By contrast to diodes on AlN templates, the ideality factor of the diodes on GaN templates was smaller, ranging from 1.6 to 2.7. Furthermore, diodes on GaN templates had a much lower series resistance, in the range of 29~190  $\Omega$ , which was due to the much larger overall GaN:Si layer thickness.

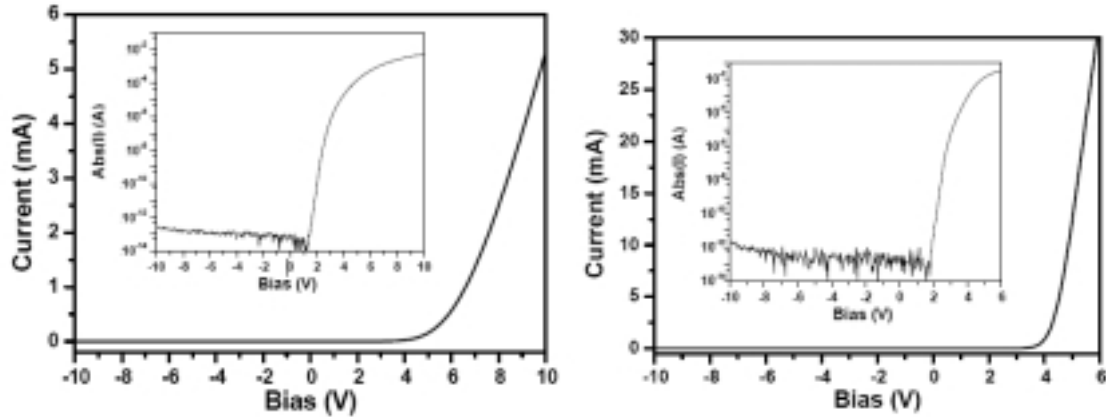
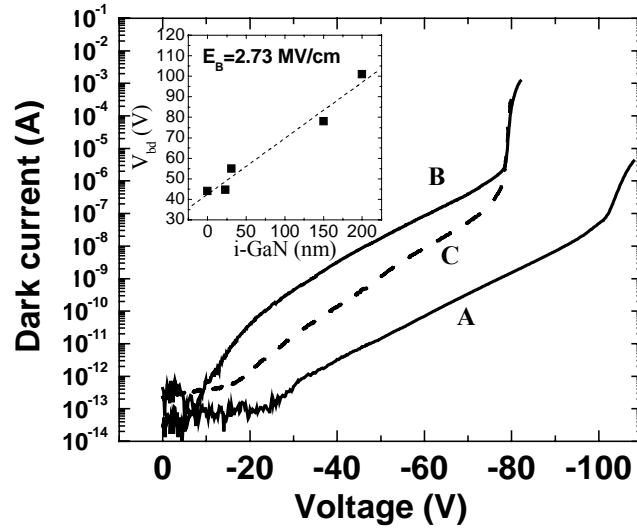


Figure 6. (Left) Current-voltage characteristics of a photodiode on AlN template (~300 nm p-GaN/150 nm i-GaN/400nm n-GaN) in linear and logarithmic scale (inset). The turn-on voltage was ~6.2 V, ideality factor was ~3.32, and series resistance was ~521  $\Omega$ . (Right) Current-voltage characteristics of a photodiode on GaN template in linear and logarithmic scale (inset). The turn-on voltage was ~4.28 V, ideality factor was ~2.45, and series resistance was ~39.4  $\Omega$ .

### 3 Carrier Multiplication in Gallium Nitride

#### 3.1 Experimental Determination of the Critical Electric Field.

$I$ - $V$  measurements were performed on the  $p$ - $i$ - $n$  diodes under high reverse biases. The breakdown characteristics were observed to vary as a function of the different layer thicknesses. Two illustrative  $I$ - $V$  characteristics under reverse bias are shown in Figure 7 for samples A ( $p$ -100 nm/  $i$ -200 nm/ $n$ -100 nm/AlN) and B ( $p$ -285 nm/  $i$ -150 nm/ $n$ -400 nm/AlN). Breakdown voltage ( $V_{bd}$ ) reduced from 102 V for sample A to 78 V for sample B, as a consequence of the narrower intrinsic region. The inset of Figure 7 shows  $V_{bd}$  as a function of  $i$ -region thickness for all the samples under study. From fitting the data with a simple abrupt junction model (assuming the potential is dropped across the intrinsic region), a critical electric field of 2.73 MV/cm is obtained; this is close to the previous values reported in the literature.[10, 11] No significant variations of the breakdown voltages were observed with the thickness of the  $p$ -type or  $n$ -type layers. Sample C ( $p$ -285 nm/  $i$ -150 nm/ $n$ -400 nm/GaN:Si/GaN) was grown at the same time as sample B; however, instead of an AlN template, a GaN:Si/GaN (2  $\mu$ m/1  $\mu$ m) template was used. It makes the effective thickness of the  $n$ -GaN layer 2400 nm. Despite this modification, it is shown that the breakdown voltage remains the same.



**Figure 7.** Breakdown characteristics of samples A, B, and C are shown. Inset: The experimental breakdown voltages obtained for different thicknesses of the intrinsic layer.

In samples A and B, the steepness of the avalanche characteristic is affected by the high series resistance created by thin  $n$ -GaN layers, and becomes softer. However, at the current levels obtained at the onset of breakdown, the effect of the series resistance is small, affecting the breakdown voltage by less than 1 V. This is shown in Figure 7, in which the device with the thinnest  $n$ -GaN layer (sample A) presents a less abrupt breakdown characteristic. This effect is a handicap for the fabrication of devices operating in Geiger mode but at the same time helps keep moderate levels of dark current above breakdown and provides a higher stability for operation in linear mode. Dark current of sample A was monitored during more than 60 h of continuous operation 2 V above the breakdown voltage, finding a standard deviation of only 6%.

### 3.2 Multiplication Gain Measurements and Determination of Ionization Coefficients.

Photocurrent measurements of samples A and B were performed under back and front illumination with a 244 nm laser (optical power=102 W/cm<sup>2</sup>). Shadowing effects of the metal contacts and probes cannot assure the same incident power for both illumination procedures; however, this is only a minor source of error for the gain of these devices. Both configurations allowed us to inject holes or electrons selectively into the active region to initiate the multiplication process. Multiplication factors were calculated from these measurements. Effects of the space-charge-region spreading with voltage were taken into account by using a one-dimensional finite element model of the device, which allowed us to fit the response at low voltages and to establish the photocurrent value corresponding to  $M=1$ . As observed in Figure 8, back illumination provides higher gain than front-illumination for both samples. The same result was obtained in all the  $p-i-n$  samples tested, regardless of the structure. Ionization events start at voltages above 50 V for holes and 70 V for electrons in sample A, and 35 and 65 V, respectively, in sample B. This agrees with the higher hole ionization coefficient that theory predicts, and which points to hole-initiated multiplication as a more beneficial concept in GaN.[12] The ionization coefficients for holes ( $\beta_p$ ) and electrons ( $\alpha_n$ ) were calculated from the multiplication factors for electrons ( $M_n$ ) and holes ( $M_p$ ) as

$\beta_p(E) = \frac{1}{W} \left( \frac{M_p(V) - 1}{M_p(V) - M_n(V)} \right) \ln \left( \frac{M_p(V)}{M_n(V)} \right)$ $\alpha_n(E) = \frac{1}{W} \left( \frac{M_n(V) - 1}{M_n(V) - M_p(V)} \right) \ln \left( \frac{M_n(V)}{M_p(V)} \right)$	<b>(Equation 2)</b> <b>Equation 2</b>
--	--

and plotted in Figure 9 assuming that the electric field ( $E$ ) is constant across the  $i$  region ( $W$ ) and equal to  $E=V/W$ . [13]

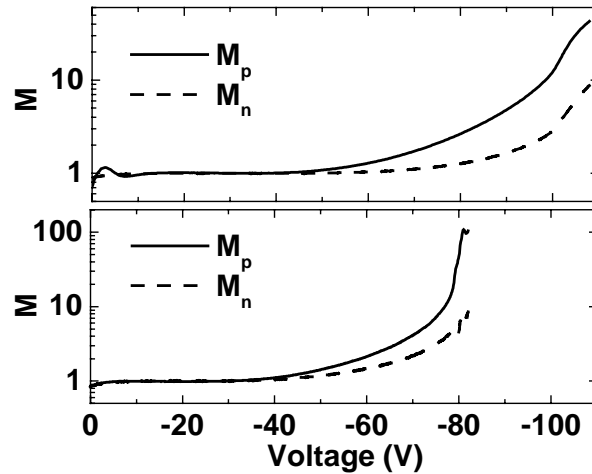


Figure 8. Multiplication factors for electrons ( $M_n$ ) and holes ( $M_p$ ) obtained from sample A (top) and sample B (bottom).

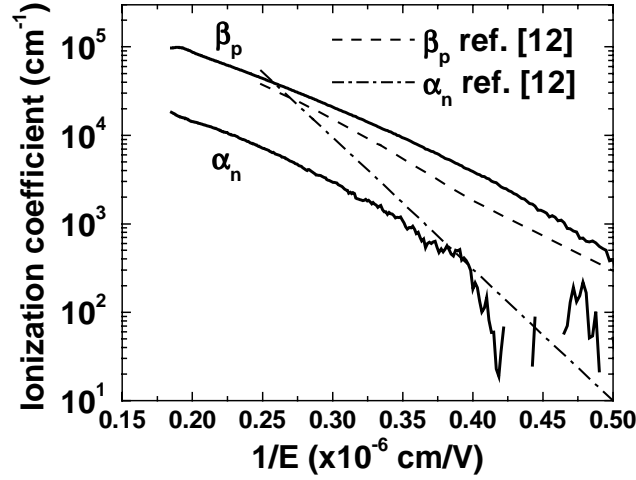


Figure 9. Solid lines: Ionization factors obtained for electrons ( $\alpha_n$ ) and holes ( $\beta_p$ ) from experiment. The dashed line and the dotted-dashed line represent theoretical values for  $\beta_p$  and  $\alpha_n$ , respectively, as extracted from Ref. 12.

### 3.3 Noise measurements.

Noise measurements were carried out on samples A and B under darkness and front and back illumination with a Xe lamp filtered at 340 nm ( $11 \text{ W/m}^2$ ). The signal from the detector was amplified with a low noise transimpedance amplifier with  $1 \times 10^7 \text{ V/A}$  before analysis using a fast Fourier transform spectrum analyzer with a 100 kHz bandwidth. The noise floor of the system was in the  $10^{-27} \text{ A}^2/\text{Hz}$  range. Results for sample A under back illumination are shown in Figure 10(a). It is noticeable that at low frequencies  $1/f$  noise dominates. Spectral power density ( $S_n$ ) for  $1/f$  noise followed the relationship  $S_n = s_0 I^2 / f^\gamma$ , with average  $s_0$  and  $\gamma$  values of  $1.4 \times 10^{-9}$  and  $\leq 0.33 \pm 0.05$ , respectively, for sample A. In sample B,  $\gamma = 1.14 \pm 0.09$  and  $s_0$  was at least three orders of magnitude higher, which suggests that the thin  $n$ -GaN plays a significant role in noise reduction. The  $\gamma$  value obtained for sample A is among the lowest values ever published in GaN. A strong reduction of  $1/f$  noise has also been observed with thin  $n$ -GaN layers in previous works.[13]

At the onset of avalanche breakdown, a white noise contribution becomes dominant in the medium frequency range (1-30 kHz). To identify the origin of that noise,  $S_n$  was plotted against current for front and back illumination (Figure 10(b)). The rapid increase of the noise level with current suggests that it is likely to be excess multiplication noise. The excess noise factor ( $F$ ) was calculated from  $F = S_n / 2qIM^2$ , where  $q$  is the electron charge,  $I$  is the current under front or back illumination, and  $M$  is the multiplication factor (inset of Figure 10.b). The results show that the excess multiplication noise factor is significantly lower under back illumination, confirming again the higher impact ionization coefficient for holes in GaN.

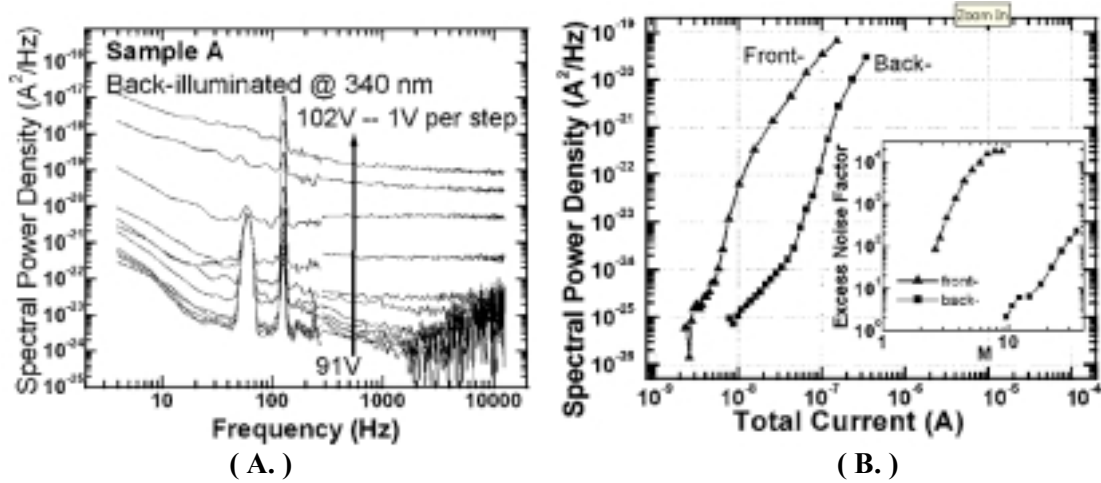


Figure 10. (a) Spectral power density ( $S_n$ ) of sample A at the onset of breakdown is shown from 91 to 102 V with 1 V steps. The two narrow spikes at 60 and 120 Hz correspond to line noise. (b) Spectral power density is plotted as a function of total current for sample A under front (triangles) and back (squares) illumination. Inset: Calculated excess noise factors for front and back illumination.

### 3.4 Summary.

In summary, multiplication and noise characteristics of back-illuminated GaN APDs have been presented and compared with those provided by front illumination. This indicated that the hole initiated multiplication yields gain and noise characteristics with superior performances. The thickness of the  $n$ -GaN layer also plays a crucial role in the design of these devices.

## 4 Linear-mode operation of back-illuminated GaN APDs

### 4.1. Scaling in back-illuminated GaN APDs.

The  $I$ - $V$  characteristics under reverse bias in dark conditions were measured for different mesa areas and geometries; this primarily allowed for the study of the dark current as a function of the mesa area while giving some insight into the effect of an increase in mesa perimeter for a fixed area.  $I$ - $V$  curves for circular mesas with increasing areas (shown in Figure 11) demonstrate a strong dependence of the dark current on the area of the device. The inset of Figure 11 displays the dark current value at a reverse bias of 70 V for increasing device areas for both square and circular mesas, demonstrating a linear increase in dark current with an increase in area. This trend, combined with the negligible differences between the dark current of square and circular mesas of the same area, suggests that the majority of the dark current can be attributed to bulk effects and agrees with the picture of a uniform distribution of higher conductivity threading dislocations across the area of the device.

The series resistances, calculated from the forward bias  $I$ - $V$  curves, range from 1.3 k $\Omega$  down to 250  $\Omega$  with increasing mesa areas from 225 to 25 000  $\mu\text{m}^2$ . These relatively high values are due to the thin  $n$ -GaN layer limiting the lateral conduction. For these back-illuminated devices, it is necessary to compromise between decreasing the thickness of the  $n$ -GaN layer in order to maximize device efficiency and increasing the thickness of the  $n$ -GaN layer in order to minimize the series resistance. Through previous studies and device modeling, we determined that a 200 nm  $n$ -GaN layer was thick enough and that current crowding is not a significant issue, while the absorption losses are low enough to achieve good device efficiencies.

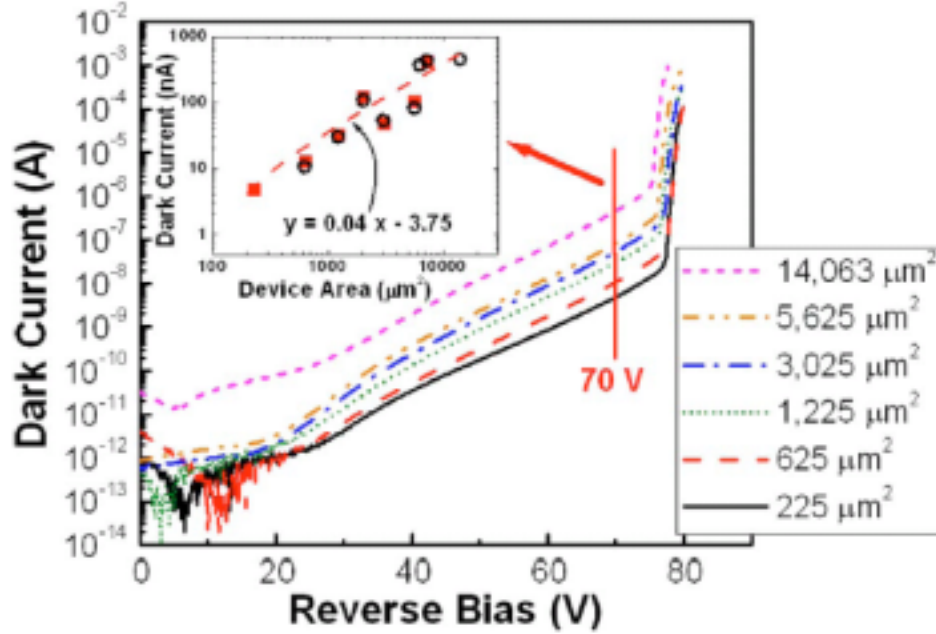


Figure 11.  $I$ - $V$  curves for circular mesa devices of increasing area. The inset plots the dark current value at 70 V reverse bias for both square (red squares) and circular (open circles) mesas with increasing area.

## 4.2. Spectral response.

The responsivity with increasing reverse bias (Figure 12) was measured under back illumination using a xenon arc lamp attached to a monochromator. The devices presented a zero-bias peak responsivity of 82 mA/W at 361 nm, with a significant decay of the response with increasing photon energy, caused by absorption in the  $n$ -GaN lateral conduction layer. The absorption coefficient in GaN scales with the photon energy, making shorter-wavelength photons more likely to be absorbed closer to the AlN interface and thus less likely to diffuse into the depletion region. As the bias increases, the response becomes flatter at short wavelengths as the depletion region expands toward the AlN interface. The increasing electric field in the depletion region also makes the long-wavelength cutoff less abrupt at higher voltages due to the Franz-Keldysh effect.[14] At the onset of breakdown, a peak responsivity of 547 mA/W at 361 nm was measured. To better differentiate the effect of this expanding depletion region and the avalanche multiplication in the device, the external quantum efficiency (EQE) of the

device was fitted at low voltage, through the use of a one-dimensional finite element model, and extrapolated to high voltages (inset of Figure 12). Thus, the EQE can be understood to increase from 29% at 0 V to 46% at 75 V, for 361 nm photons.

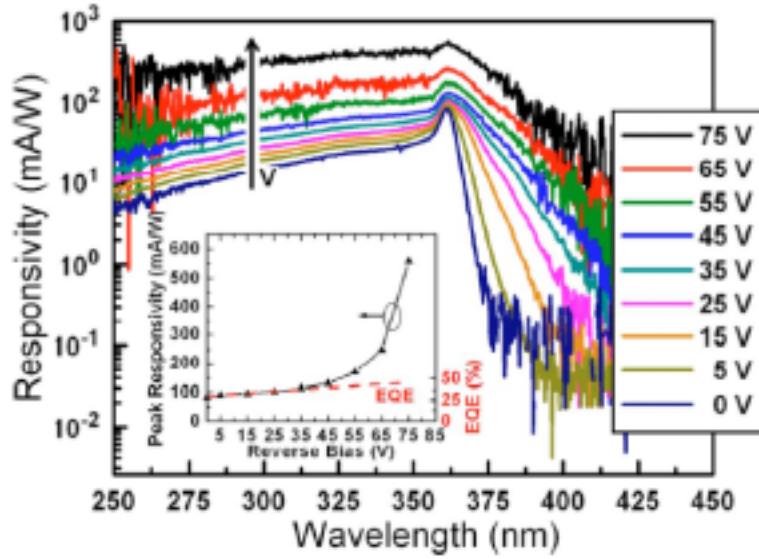


Figure 12. Responsivity measurements with increasing reverse bias. The inset plots the peak responsivity with increasing bias and the extracted external quantum efficiency fit.

#### 4.3. Avalanche Gain Uniformity.

The gain characteristics of several devices were determined by measuring the light and dark  $I$ - $V$  curves under reverse bias and subtracting them to obtain the photocurrent. For light current measurements, the back side of the device was illuminated with a frequency-doubled argon ion laser at 244 nm (optical power= $76.4 \text{ mW/cm}^2$ ). For each calculated gain curve, the light and dark  $I$ - $V$  curves were alternatively measured three times in a row to ensure consistent device operation. The gain is determined by normalizing the photocurrent at the onset of gain ( $M=1$ ); the onset of gain is determined following a similar procedure as used to calculate the EQEs, allowing the establishment of the photocurrent value corresponding to  $M=1$ . Figure 13(a) displays the light and dark current curves around breakdown, along with the resulting gain, from circular devices with areas of 625, 3025, and 14 063  $\mu\text{m}^2$ . From these measurements, a very sharp increase in gain at breakdown is observed, and maximum gains of 5700, 1500, and 760, at  $\sim 81 \text{ V}$  reverse bias are demonstrated for the 625, 3025, and 14 063  $\mu\text{m}^2$  devices, respectively. Figure 13(b) displays the gain curves for increasing mesa areas, demonstrating uniform gain behavior with area. There is a slight variation in breakdown voltage; however, there is no trend with area, and therefore this is attributed primarily to material uniformity.

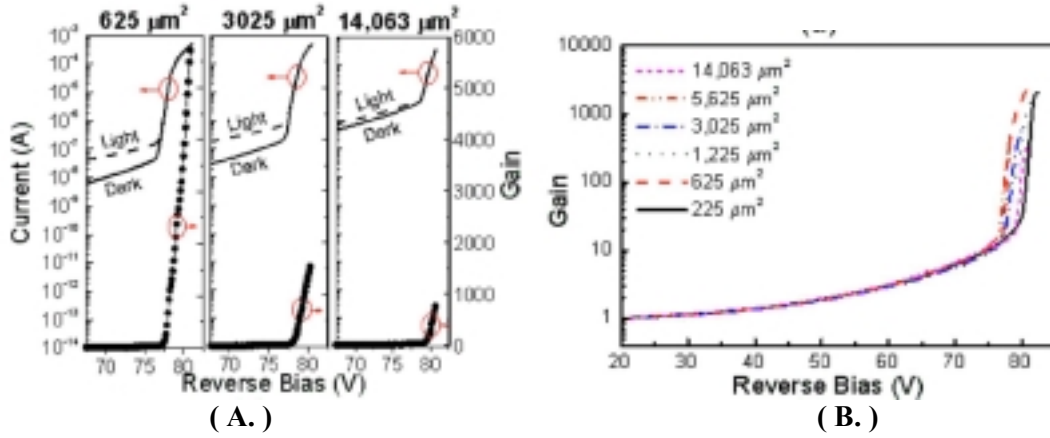


Figure 13. (a) Light current, dark current, and gain curves around breakdown from 625, 3025, and 14 063 μm² avalanche photodiodes. (b) Gain vs reverse bias for several mesa areas.

To determine the amount of dark current which experiences avalanche multiplication, the dark current was expressed as  $I_{\text{dark}} = I_{\text{multiplied}}M + I_{\text{unmultiplied}}$  and a plot of  $M$  vs  $I_{\text{dark}}$  was utilized to determine  $I_{\text{multiplied}}$ , which was then plotted as a function of mesa area (Figure 14). The 225 μm² mesa has an  $I_{\text{multiplied}}$  of 3 nA, which increases linearly up to a value of 400 nA for a mesa area of 7 225 μm².

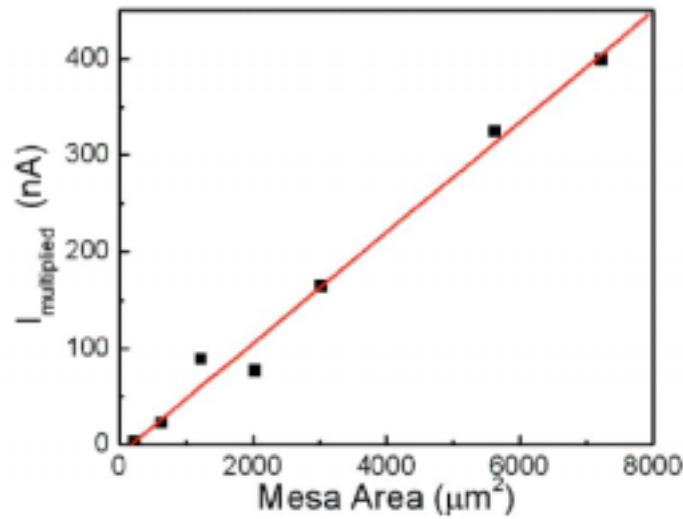


Figure 14. Multiplied current component of the dark current as a function of mesa area.

#### 4.4. Temperature dependence of the breakdown voltage.

In order to confirm that the gain is the result of avalanche breakdown in the largest area devices, the breakdown characteristics were studied as a function of temperature. Figure 15 displays the dark I-V curves around the breakdown voltage at temperatures ranging from 250 up to 564 K for a 14 063 μm² diode, which shows a clear increase in breakdown voltage with temperature. The inset plots the breakdown voltage



as a function of temperature, demonstrating a linear behavior with a positive thermal coefficient of +8.3 mV/K, comparable to other reported values.[15, 16] A similar value was obtained for the 25 000  $\mu\text{m}^2$  devices, indicating that the thermal coefficient does not appear to scale with area. The general increase in the dark current with temperature is thought to be a thermally activated process. A linear fit to an Arrhenius plot of the dark current at 70 V reverse bias as a function of temperature gave an activation energy of 0.13 eV.

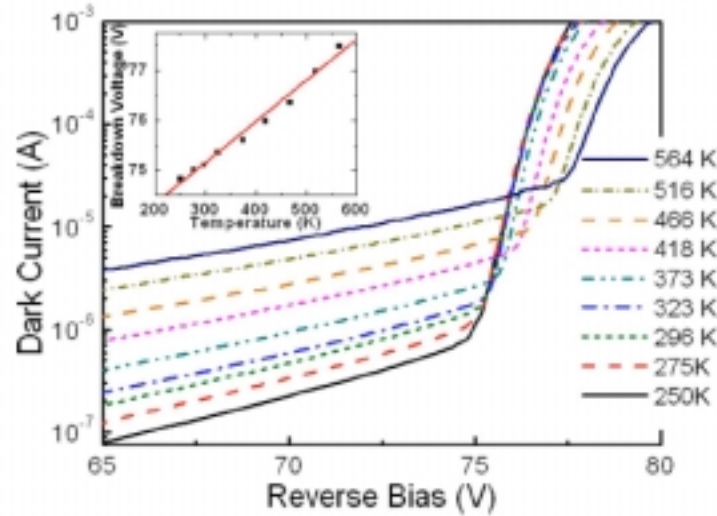


Figure 15. Temperature-dependent evolution of the breakdown from 250 to 564 K for a 14 063  $\mu\text{m}^2$  device. The inset plots temperature vs breakdown voltage demonstrating a positive thermal coefficient of +8.3 mV/K.

#### 4.5. Summary.

Scaling effects in back-illuminated GaN APDs have been studied. With an increase in size, it was found that the dark current increases, indicating bulk leakage as the dominant contribution to the dark current. The responsivity was studied as a function of reverse bias, demonstrating a flatter response at higher voltages. The gain curves were found to be uniform with increasing device area. The multiplied component of the dark current increases linearly with an increase in mesa area. Temperature-dependent measurements were used to confirm the avalanche process in large area devices.

## 5 Geiger-mode operation of back-illuminated GaN APDs

### 5.1 Experimental Set-Up.

A Xe lamp and a monochromator were used to illuminate the devices within the 230–450 nm range. The light was coupled into the device through an UV fiber-optic cable. The input slit of the monochromator was adjusted to vary the photon flux, which was calibrated using a NIST traceable Si detector. The APDs were measured in Geiger mode with a gated quenching circuit, as shown in Figure 16(a). A reverse dc voltage ( $V_{dc}$ ) between 74 and 78 V was applied to the APD through a 47 k $\Omega$  resistor biasing the device just below breakdown, and a pulsed excess voltage ( $\Delta V_p$ ) between 8.5 and 10 V was coupled through a 50 nF capacitor to bias the device above breakdown. Pulse repetition rate was 10 kHz with a pulse width of 10 ns and a dead time of

100  $\mu\text{s}$ . The photocurrent pulses were examined using an oscilloscope to measure the voltage drop across a 50  $\Omega$  load resistor. Although 50  $\Omega$  matching cables were used, some ringing was still evident after the 10 ns pulse, primarily due to the mismatch between the device impedance and the output of the pulse generator. Figure 16(b) shows the photocurrent pulses obtained at different wavelengths in a 5625  $\mu\text{m}^2$  area device under back illumination with a flux of ten photons per pulse. For wavelengths less than the absorption cutoff, photocurrent pulses close to 0.6 mA are generated under illumination corresponding to an effective gain of about  $10^7$ , while beyond the cutoff, a negligible photocurrent pulse is observed. A Stanford Research model SR400 photon counter was employed to discriminate and count the photon pulses. The discriminator voltage was established to maximize the detection efficiency while minimizing the number of spurious dark counts.

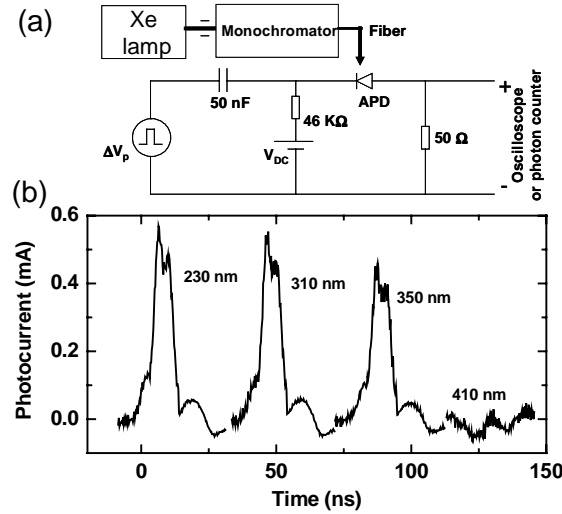


Figure 16. (a) Gated quenching circuit and optical setup for Geiger-mode operation. (b) Photocurrent pulses obtained in a 5625  $\mu\text{m}^2$  area device at different wavelengths with a  $V_{dc}$  of 75 V and a  $\Delta V_p$  of 8.5 V.

## 5.2 Spectral Response.

In order to further investigate the spectral response in photon counting mode and the uniformity of that response, four different 625  $\mu\text{m}^2$  area devices were scanned from 230 to 400 nm with a photon flux of about one photon per pulse. The average SPDE as a function of wavelength is shown with error bars in Figure 17. Reasonably flat detection efficiency was obtained for photon energies above the band gap; below the band gap, a sharp cutoff and a high visible light rejection ratio are observed. As shown in the inset of Figure 17, the detection cutoff is shifted to the left in comparison to the transmission cutoff, both in the unbiased case and near breakdown, under the application of 75 V reverse bias. The reason for this shift is the sharp change in the photon penetration depth close to band gap edge. Photons with energies close to the band gap have more probability of generating electron-hole pairs in the space charge region (SCR), in contrast to those with energies well above the band gap, which are more likely to be absorbed in the neutral portion of the  $n$ -type GaN region. The absorption of photons in the SCR increases the electron-initiated ionization in the multiplication region. Hence, the lower

ionization coefficient for this type of carrier leads to smaller photocurrent pulses near the band gap, as shown in Figure 16, for 350 nm photons. The discriminator circuit can then fail to register the smaller pulses, producing a shift in the spectral response.

**Figure 17. Spectral response of a 625  $\mu\text{m}^2$  area device obtained at a  $V_{dc}$  of 77 V and a  $\Delta V_p$  of 10 V. Inset: spectral response in linear scale and transmission measurements at 0 and -75 V.**

### **5.3 *Single Photon Detection Efficiency and Dark Count Rate.***

The pulse detection efficiency was investigated as a function of the photon flux in order to identify the minimum photon flux for effective operation. Figure 18(a) shows how, as the device size increases, the photon flux needed to have a 100% probability of having a count per pulse also increases. Single photon detection efficiencies (SPDEs) and dark count rates were measured in devices with areas up to 14 063  $\mu\text{m}^2$ . Figure 18(b) shows their average values obtained from measurements of three different devices for each APD area under illumination at 340 nm with a flux of one photon per pulse. The detectors with areas of 225 and 625  $\mu\text{m}^2$  presented SPDEs of 20% and 15.3%, respectively, with a dark count rate below the measurement limit (<10 kHz). Although a possible contribution from after pulsing cannot be completely ruled out, this low dark count rate suggests that the effect of thermal and tunneling processes on the pulse count is significantly reduced in the small area devices.

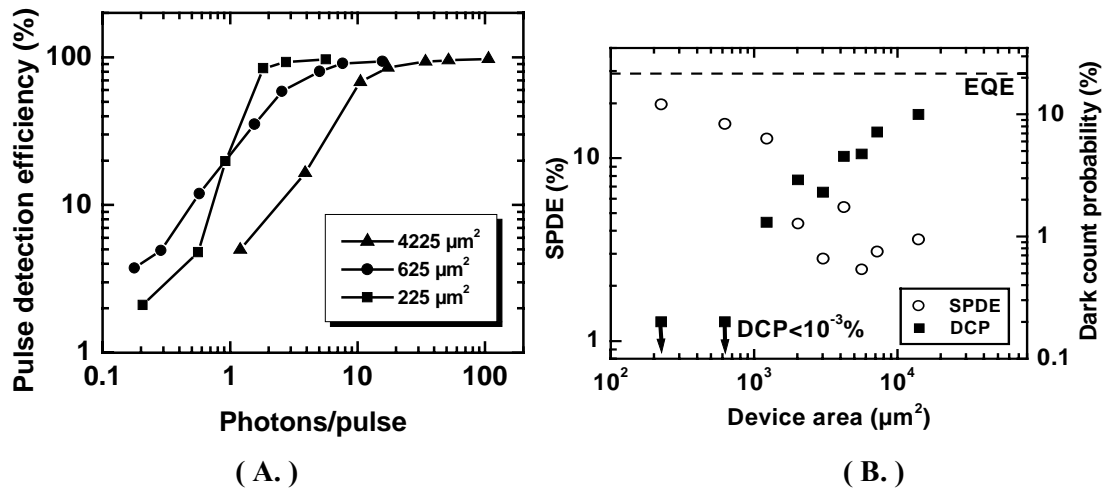


Figure 18. (a) Pulse detection efficiency measured as a function of photon flux for devices with 4225, 625, and 225  $\mu\text{m}^2$  areas. (b) SPDE (left axis) and dark count rate (right axis) achieved under 340 nm illumination in devices with sizes ranging from 225 to 14 063  $\mu\text{m}^2$ . The straight line indicates the limit based on the maximum EQE achievable at 340 nm under bias.

## 5.4 Summary.

Back-illuminated GaN APDs operating in Geiger mode have been presented. These devices showed a flat Geiger-mode response for photon energies above the band gap and a high visible-light rejection ratio. Single photon counting was demonstrated in devices ranging from 225 all the way up to 14 063  $\mu\text{m}^2$ . In the smallest device, SPDE of 20% and the dark count rate <10 kHz were obtained.

## 6 Publications Resulting From This Project

1. **Scaling in back-illuminated GaN avalanche photodiodes**  
K. Minder, J.L. Pau, R. McClintock, P. Kung, C. Bayram, M. Razeghi and D. Silversmith  
Applied Physics Letters, Vol. 91, No. 7, p. 073513-1-- **August 13, 2007**
2. **Geiger-mode operation of back-illuminated GaN avalanche photodiodes**  
J. L. Pau, R. McClintock, K. Minder, C. Bayram, P. Kung, M. Razeghi, E. Muñoz, and D. Silversmith  
Applied Physics Letters, Vol. 91, No. 04, p. 041104 -1-- **July 23, 2007**
3. **Hole-initiated multiplication in back-illuminated GaN avalanche photodiodes**  
R. McClintock, J.L. Pau, K. Minder, C. Bayram, P. Kung and M. Razeghi  
Applied Physics Letters, Vol. 90 No. 14, p. 141112-1-- **April 2, 2007**
4. **III-Nitride Avalanche Photodiodes**  
P. Kung, R. McClintock, J. Pau Vizcaino, K. Minder, C. Bayram and M. Razeghi

## 7 References

---

1. I. Prochazka, K. Hamal, and B. Sopko, J. Mod. Opt. 51, 1289 (2004).
2. B. F. Aull, A. H. Loomis, D. J. Young, R. M. Heinrichs, B. J. Felton, P. J. Daniels, and D. J. Landers, Lincoln Lab. J. 13, 335 (2002).
3. M. Razeghi, A. Yasan, R. McClintock, K. Mayes, D. Shiell, S. R. Darvish, and P. Kung, Phys. Status Solidi C 1, S141 (2004).
4. E. Muñoz, E. Monroy, J. L. Pau, F. Calle, F. Omnès, and P. Gibart, J. Phys.: Condens. Matter 13, 7115 (2001).
5. K. A. McIntosh, R. J. Molnar, L. J. Mahoney, K. M. Molvar, N. Efremow, Jr., and S. Verghese, Appl. Phys. Lett. 76, 3938 (2000).
6. A. L. Beck, X. Guo, H.-D. Liu, A. Ghatak-roy, and J. C. Campbell, Proc. SPIE 6372, 63720O-1 (2006).
7. J. Zhang, H. Wang, W. Sun, V. Adivarahan, S. Wu, A. Chitnis, C. Chen, M. Shatalov, E. Kuokstis, J. Yang, and M. Asif Khan, J. Elect. Mat. 32, 364 (2003).
8. P. Kung, C.J. Sun, A. Saxler, H. Ohsato, and M. Razeghi, J. Appl. Phys. 75, 4515 (1994).
9. C.J. Sun, P. Kung, A. Saxler, H. Ohsato, K. Haritos, and M. Razeghi, J. Appl. Phys. 75, 3964 (1994).
10. A. Nishikawa, K. Kamakura, T. Akasaka, and T. Makimoto, Appl. Phys. Lett. 88, 173508 (2006).
11. X. A. Cao, H. Lu, S. F. LeBoeuf, C. Cowen, S. D. Arthur, and W. Wang, Appl. Phys. Lett. 87, 053503 (2005).
12. I. J. Oguzman, E. Belotti, K. F. Brennan, J. Kolnik, R. Wang, and P. P. Ruden, J. Appl. Phys. 81, 7827 (1997).
13. G. Stillman and C. Wolfe, in *Semiconductors and Semimetals*, edited by R. Willardson (Academic, New York, 1977), Vol. 12, Chap. 5, p. 333.
14. K. A. McIntosh, R. J. Molnar, L. J. Mahoney, A. Lightfoot, M. W. Geis, K. M. Molvar, I. MeIngailis, R. L. Aggarwal, W. D. Goodhue, S. S. Choi, D. L. Spears, and S. Verghese, Appl. Phys. Lett. 75, 3485 (1999).
15. B. Yang, T. Li, K. Heng, C. Collins, S. Wang, J. C. Carrano, R. D. Dupuis, J. C. Campbell, M. J. Schurman, and I. T. Ferguson, IEEE J. Quantum Electron. 36, 1389 (2000).

- 
16. J. B. Limb, D. Yoo, J. H. Ryou, W. Lee, S. C. Shen, R. D. Dupuis, M. L. Reed, C. J. Collins, M. Wraback, D. Hanser, E. Preble, N. M. Williams, and K. Evans, Appl. Phys. Lett. 89, 01112 (2006).